RSC Advances

PAPER

View Article Online
View Journal | View Issue



Cite this: *RSC Adv.*, 2024, **14**, 40077

# Tunable band alignment and large power conversion efficiency in a two-dimensional InS/$ZnIn_2S_4$ heterostructure†

Hui-Ying Liu,[a] Heng-Fu Lin, *[ab] Lu-Ya Xu,[a] Ting-Ping Hou[ab] and Nan-Shu Liu*[c]

Heterostructures can efficiently modulate the bandgap of semiconductors and enhance the separation of photocarriers, thereby enhancing the performance of optoelectronic devices. Herein, we design an InS/$ZnIn_2S_4$ van der Waals (vdW) heterostructure and investigate its electronic and photovoltaic properties using first principles calculation. Compared to its individual monolayers, the InS/$ZnIn_2S_4$ heterostructure not only possesses a smaller band gap of 2.21 eV and superior light absorption performance in the visible short-wavelength region (<500 nm) but also forms a type-$II_1$ band alignment. Moreover, a large power conversion efficiency (PCE) of 10.86% is achieved. The transformation of the band alignment from type-$II_1$ to type-I or type-$II_2$ can be forced using an external electric field, and the PCE can be further increased up to 12.19% at a positive $E_\perp$ of 0.2 V $Å^{-1}$. Within a critical biaxial strain of 4%, the type-$II_1$ band alignment can be maintained, and a high PCE of 20.80% is achieved at a tensile strain ($\varepsilon$) of 4%. Our results may suggest a potential optoelectronic application direction for the InS/$ZnIn_2S_4$ heterostructure and offer effective means to enhance its optoelectronic device performance.

Received 25th September 2024
Accepted 6th December 2024

DOI: 10.1039/d4ra06901c

rsc.li/rsc-advances



## 1. Introduction

Nowadays, in the face of increasing global energy shortages and environmental pollution, finding new green energy sources to replace traditional fuels has become a pressing issue, including solar energy, ocean energy, wind energy, biomass energy, and so on.[1] Solar cells made of materials with specific photovoltaic properties can directly convert solar energy into electricity, which has become the main idea of the next generation of green power generation.[2] Power conversion efficiency (PCE) is a metric that quantifies the efficiency with which a solar cell converts incident solar energy into useable electrical power. To enhance the PCE of solar cells, we can either employ high-quality photovoltaic materials (Si, CdSe, GaSe, and perovskite materials) with a wide spectral absorption range[3,4] or create a heterojunction using two different semiconductor materials to increase the efficiency of the separation of photogenerated electrons and holes and to prolong the life time of the carriers.[5,6]

As we know, heterostructures can integrate the advantages of their individual constituent materials to overcome limitations, further enhancing their existing properties and expanding their applications.[3,4,7–11] Heterostructures with type-II band alignment are commonly utilized in photocatalytic water splitting and photovoltaic devices.[12,13]

Since the emergence of graphene,[14] two-dimensional (2D) materials and their heterostructures have garnered considerable attention owing to their unique physical properties and applications in novel optoelectronic devices.[3,5,6,15–20] In recent years, solar cells constructed with 2D semiconductors heterostructures have received extensive theoretical and experimental research.[6,20–22] Using polymer stacking and chemical vapor deposition (CVD), a graphene/$WS_2$ heterostructure,[23] $WSe_2$/$MoS_2$ heterostructure,[24] $WSe_2$/$MoSe_2$ heterostructure,[25] and p-Si/$MoS_2$ heterostructure[26] have been successfully prepared and exhibited a photoelectric conversion efficiency ranging from 0.12% to 5.23%. Furthermore, 2D GaX/$SnS_2$ (X = S or Se), GaS/$SnS_2$, Janus $Ga_2SeTe$/InS, and $SbI_3$/$BiI_3$ heterostructures have been theoretically proposed for solar cells with a considerable PCE.[4,6,27] Under atom doping, compressive strain, or an electric field, their PCE can reach up to 16.47%, 23.2%, and 21.63%, respectively.

Recently, a new family of 2D binary semiconductors, metal monochalcogenides MX (M = Ga, In; X = S, Se, Te), have garnered considerable interest because of their excellent physicochemical properties.[28,29] The monolayer MX can be synthesized through mechanical exfoliation methods[30,31] and vapor phase transport approach.[32,33] MX monolayers have an indirect

[a]*Hubei Province Key Laboratory of Systems Science in Metallurgical Process, College of Science, Wuhan University of Science and Technology, Wuhan 430081, China. E-mail: hflin@wust.edu.cn*

[b]*The State Key Laboratory for Refractory Material and Metallurgy, International Research Institute for Steel Technology, Collaborative Center on Advanced Steels, Wuhan University of Science and Technology, Wuhan 430081, China*

[c]*Chongqing Key Laboratory of Micro & Nano Structure Optoelectronics, School of Physical Science and Technology, Southwest University, Chongqing 400715, China. E-mail: liuns0215@gmail.com*

† Electronic supplementary information (ESI) available. See DOI: https://doi.org/10.1039/d4ra06901c

bandgap between 2.0 eV and 4.0 eV, and their band structure and optical absorption spectrum can be effectively modulated by layer thickness[34,35] and nanofabrication.[36] The InS monolayer and its heterostructure InS/InSe have been widely studied, possessing a PCE of 13.7%.[37] Besides the binary metal monochalcogenides MX, the ternary metal chalcogenide semiconductor $ZnIn_2X_4$ (X = S, Se, Te) has also garnered significant interest owing to its excellent light absorption performance, and remarkable thermal and chemical stability.[38,39] $ZnIn_2S_4$ nanosheets have now been synthesized and used for efficient photocatalytic hydrogen evolution, solar-powered $CO_2$ conversion and hydrogen evolution reactions.[40,41] In addition, many $ZnIn_2X_4$-based heterostructures have been fabricated and proposed for photodetectors, high-efficiency solar cells, and photocatalytic hydrogen evolution, such as O-SnS/I-$ZnIn_2S_4$,[42] $ZnIn_2S_4$/$ZnIn_2Se_4$($ZnIn_2Se_4$/$ZnIn_2Te_4$),[43] and $ZnIn_2S_4$/$SnSe_2$.[44] Considering this, one intriguing question is whether the InS/$ZnIn_2S_4$ heterostructure could exhibit better electronic and optical properties, potentially leading to improved photovoltaic performance.

In this paper, firstly, we theoretically design the InS/$ZnIn_2S_4$ heterostructure and present a detailed study of its electronic and optical properties, including electronic structure, band alignment, optical absorption coefficients and PCE. It is found that the InS/$ZnIn_2S_4$ heterostructure possesses an indirect bandgap of 2.21 eV, a type-$II_1$ band alignment, a large optical absorption coefficient, and a significant PCE of 10.86%. Next, the effects of an external field (electrical field and strain) on the band alignment and PCE of the InS/$ZnIn_2S_4$ heterostructure are also investigated. The band alignment transitions from type-$II_1$ to type-I, type-$II_2$ or type-III under an external electrical field, while it always stays in type-$II_1$ under a biaxial strain. The PCE will increase to 12.19% at an external electric field of 0.2 V Å$^{-1}$, and to 20.80% at a tensile strain of $\varepsilon = 4\%$.

## 2. Methods

All calculations are carried out using the Vienna *Ab initio* Simulation Package (VASP),[45,46] employing density functional theory (DFT). The exchange-correlation effect are treated with the generalized gradient approximation (GGA) of the Perdew–Burke–Ernzerhof (PBE) functional,[47] within the projector augmented wave (PAW) framework.[48,49] A plane wave cutoff energy of 450 eV is used. Geometric relaxation is performed until the residual force on each atom is below 0.01 eV Å$^{-1}$. The Brillouin zone integration was sampled using 10 × 10 × 1 *k*-point meshes generated by the Monkhorst–Pack scheme.[50] The electronic structure is also calculated using the Heyd–Scuseria–Ernzerhorf (HSE06) hybrid functionals.[51] van der Waals (vdW) interactions between layers in the heterostructure are accounted for using a DFT-D2 approach.[52] To eliminate spurious periodic interactions, a vacuum layer of 15 Å was introduced along the direction perpendicular to the heterostructure.

The binding energy $E_b$ is calculated to assess the energy stability of the InS/$ZnIn_2S_4$ heterostructure, which is defined as the following equation,

$$E_b = E_{InS/ZnIn_2S_4} - E_{InS} - E_{ZnIn_2S_4}$$

where $E_{InS/ZnIn_2S_4}$ denotes the total energy of the InS/$ZnIn_2S_4$ heterostructure, while $E_{InS}$ and $E_{ZnIn_2S_4}$ represent the total energies of the isolated InS and $ZnIn_2S_4$ monolayers, respectively.

Both the optical absorption coefficient $\alpha(\omega)$ and PCE are also calculated to quantitatively analyze the optical properties of the InS/$ZnIn_2S_4$ heterostructure. The $\alpha(\omega)$ is computed from the following equation,[53]

$$\alpha(\omega) = \sqrt{2}\omega\left[\sqrt{\varepsilon_1{}^2(\omega) + \varepsilon_2{}^2(\omega)} - \varepsilon_1(\omega)\right]^{1/2}$$

where $\varepsilon_2(\omega)$ represents the imaginary part of the dielectric function, and $\varepsilon_1(\omega)$ is the real part of the dielectric function, derived from $\varepsilon_2(\omega)$ through the Kramers–Kronig transformation. The PCE is defined as follows,[54]

$$\eta = \frac{J_{SC} V_{OC} \beta_{FF}}{P_{solar}} = \frac{0.65\left(E_g^d - \Delta E_c - 0.3\right)\int_{E_g^d}^{\infty} (P(\hbar\omega)/\hbar\omega)d(\hbar\omega)}{\int_0^{\infty} P(\hbar\omega)d(\hbar\omega)}$$

where $\beta_{FF}$, $V_{OC}$, $J_{SC}$, and $P_{solar}$ represent the band-fill factor, maximum open-circuit voltage, short-circuit current, and sum of the AM1.5 incident solar irradiation, respectively. $\beta_{FF}$ is typically assigned a value of 0.65,[54] $V_{OC} = E_g^d - \Delta E_c - 0.3$, and $P_{solar} = \int_0^{\infty} P(\hbar\omega)d(\hbar\omega)$. In addition, $E_g^d$, $\Delta E_c$, $P(h\omega)$, and $h\omega$ represent the donor layer's bandgap, conduction band offset (CBO) of the heterostructure, AM1.5 solar energy flux, and photon energy, respectively.

The carrier mobility for the InS/$ZnIn_2S_4$ van der Waals (vdW) heterostructure can be approximated using the deformation potential model, which is expressed as,[55,56]

$$\mu_{2D} = \frac{e\hbar^3 C_{2D}}{k_B T m^* \overline{m} E_1{}^2}$$

where $e$ is the electron's charge, $h$ is the reduced Planck constant, $C_{2D}$ is the elastic modulus, $k_B$ is the Boltzmann constant, $T$ is the temperature set to 300 K, $m^* = \hbar^2\left(\frac{\partial^2 E(k)}{\partial k^2}\right)^{-1}$ is the carrier effective mass, $\overline{m} = \sqrt{m_x^* m_y^*}$ is the average carrier effective mass, and $E_l = \frac{\partial E_{edge}}{\partial \varepsilon}$ is the deformation potential constant, where $E_{edge}$ represents the band edge energy of the electrons and holes produced by the infinitesimal uniaxial strain $\varepsilon$, along the armchair and zigzag directions.

## 3. Results and discussion

The crystal structure and band structure of the isolated InS and $ZnIn_2S_4$ monolayers are displayed in Fig. S1.† The monolayer InS has a hexagonal lattice and four atomic-layer structure with a unit cell containing two In and two S atoms. The lattice constants of InS are $a_{InS} = b_{InS} = 3.93$ Å. The valence band maximum (VBM) is along the $\Gamma$–M line, while the conduction

 

band minimum (CBM) is at $\Gamma$ point, indicating that InS is an indirect band gap semiconductor. The band gap of InS is calculated to be 1.66 eV under the PBE functional level and 2.47 eV under the HSE06 functional level, consistent with previous reports.[28] The monolayer $ZnIn_2S_4$ forms a rectangular lattice and seven atomic-layer structure with a unit cell containing two Zn, four In and eight S atoms. The lattice constants of $ZnIn_2S_4$ are $a_{ZnIn_2S_4} = 6.78$ Å and $b_{ZnIn_2S_4} = 3.93$ Å. The CBM and VBM are both situated at the Γ point, which means that it is a direct band gap semiconductor. The calculated band gap of $ZnIn_2S_4$ is 1.79 eV under the PBE functional level and 2.73 eV under the HSE06 functional level, consistent with a previous study.[39] Moreover, for both InS and $ZnIn_2S_4$ monolayers, the HSE06 functional only increased the bandgap and did not change the general shape of the band structure. For all subsequent calculations, we only use the HSE06 functional.

To construct a two-dimensional InS/$ZnIn_2S_4$ heterostructure with a small lattice mismatch,[57,58] a $\sqrt{3} \times 1$ supercell of the isolated InS monolayer and a unit cell of $ZnIn_2S_4$ monolayer are selected. The lattice mismatch is determined using the following formula $[(a_{ZnIn_2S_4} - \sqrt{3}\, a_{InS})/a_{ZnIn_2S_4}] \times 100\%$ for the $x$ direction and $[(b_{ZnIn_2S_4} - b_{InS})/b_{ZnIn_2S_4}] \times 100\%$ for the $y$ direction, and the corresponding mismatch values are 0.14% and 0%, respectively. Then, to determine the energetically favorable structure of the InS/$ZnIn_2S_4$ heterostructures, we consider four representative heterostructures formed with different stacking configuration, specifically AA, AB, AC and AD, as shown in Fig. 1. The equilibrium structural parameters (lattice parameters $a$ and $b$, interlayer distance $d$) and binding energy $E_b$ of the four configurations of the InS/$ZnIn_2S_4$ heterostructures are listed in Table S1.† These four heterostructures have nearly identical lattice parameters of $a \approx 6.80$ Å and $b \approx 3.93$ Å, which closely resemble the dimensions of the unit cell of the isolated $ZnIn_2S_4$ (or $\sqrt{3} \times 1$ supercell of the isolated InS monolayer). The calculated interlayer distances $d$ of the InS/$ZnIn_2S_4$ heterostructures with AA, AB, AC, and AD stacking are 3.71, 3.77, 4.19, and 4.03 Å, respectively. All four stacking configurations are energetically stable, as their binding energies $E_b$ are negative.[59] The InS/$ZnIn_2S_4$ heterostructure with AA stacking is the most energetically favorable, since it has the smallest binding energy. To evaluate the dynamic and thermal stability of the InS/$ZnIn_2S_4$ heterostructure, the phonon spectrum was obtained and molecular dynamics simulations are also performed. The phonon dispersion does not have an imaginary mode, as shown in Fig. S4(a),† which indicates that the heterostructure is dynamically stable. The fluctuations of the total energy of the InS/$ZnIn_2S_4$ heterostructure at room temperature (300 K) as a function of time is depicted in Fig. S4(b).† The results suggest that the heterostructure is thermally stable at room temperature, since the fluctuation of the total energies is small. In addition, the AA stacking configuration has the smallest interlayer distance $d$. In subsequent studies, we mainly focus on the AA stacking configuration.

Fig. 2(a) shows the charge density difference $\Delta\rho$, defined as $\Delta\rho = \rho_{InS/ZnIn_2S_4} - \rho_{InS} - \rho_{ZnIn_2S_4}$. Here, $\rho_{ZnIn_2S_4}$, $\rho_{InS}$, and $\rho_{ZnIn_2S_4}$ represent the charge density of the InS/$ZnIn_2S_4$ heterostructure, isolated InS, and isolated $ZnIn_2S_4$, respectively. The planar-averaged charge density difference $\Delta\rho(z)$, defined as $\Delta\rho(z) = \frac{1}{A_{xy}} \int \Delta\rho dxdy$, is also displayed in Fig. 2(a). Here, $A_{xy}$ represents the surface area of the InS/$ZnIn_2S_4$ heterostructures.[60] The curves of $\Delta\rho(z)$ were oscillated, and the amplitude of the oscillations experiences a notable surge in proximity to the interface, indicating that charge transfer and

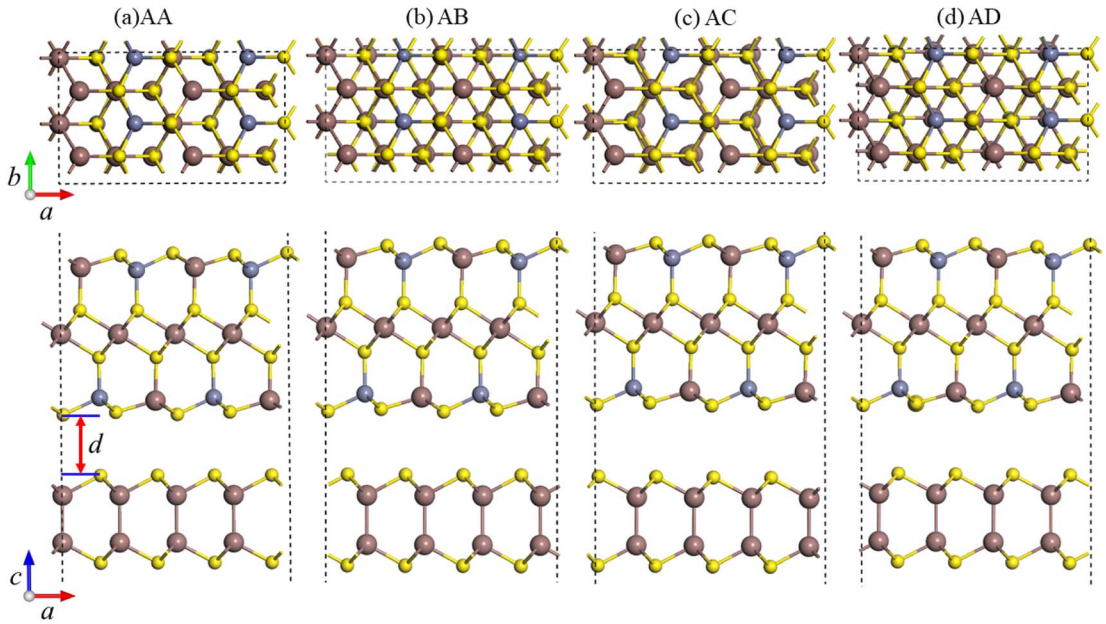


Fig. 1 Top and side views of the four possible stacking configurations of the InS/$ZnIn_2S_4$ heterostructures: (a) AA, (b) AB, (c) AC, and (d) AD. $d$ represents the interlayer distance.

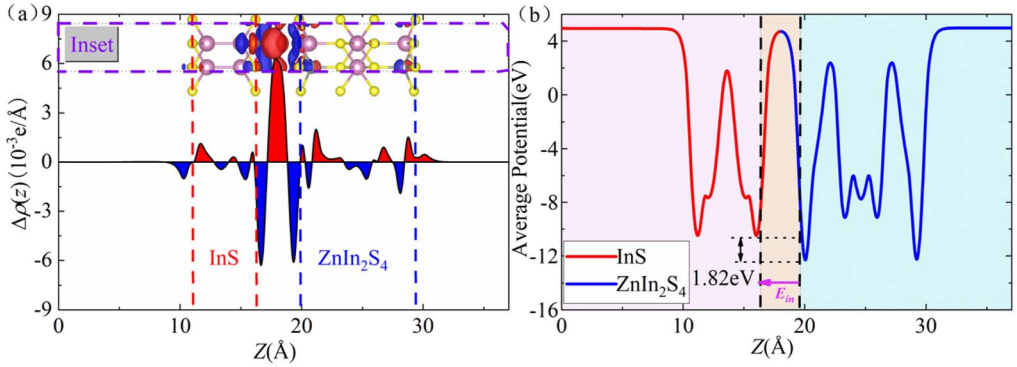


Fig. 2 (a) The planar-averaged charge density difference $\Delta\rho(z)$ of the InS/$ZnIn_2S_4$ heterostructure (inset: three-dimensional charge density difference $\Delta\rho$). Red regions indicate electron accumulation, while blue regions signify electron depletion. (b) The planar-averaged electrostatic potential of the InS/$ZnIn_2S_4$ heterostructure along the $z$-axis. The potential drop $\Delta V$ at the interface is 1.82 eV. The pink arrow indicates the direction of the built-in electric field.

rearrangement occur within the interfacial region of the InS/$ZnIn_2S_4$ heterostructure. In addition, from the three-dimensional charge density difference $\Delta\rho$, we find that the electrons primarily accumulate in the vdW gap between the InS and $ZnIn_2S_4$ layers, while the electron-deficient regions predominantly occur around the interface S atoms of both InS layer and $ZnIn_2S_4$ layer. Furthermore, Bader charge analysis indicates that there is a charge transfer of about 0.004$e$ that occurs from the $ZnIn_2S_4$ layer to the InS layer. This can induce a weak effective built-in electric field ($E_{in}$) at the interface that is directed from the $ZnIn_2S_4$ layer toward the InS layer,[61,62] as shown by the pink arrow in Fig. 2(b). Fig. 2(b) shows the planar-averaged electrostatic potential $V$ profiles along the $z$-axis, from which $E_{in}$ can be inferred based on the potential drop $\Delta V$ at the interface of the heterostructure. This electric field plays a crucial role in facilitating the separation of photoinduced electron–hole pairs, thereby prolonging the lifetimes of carriers in the heterostructure. In addition, we calculated the carrier mobility of the InS/$ZnIn_2S_4$ heterostructure. Table S4† lists the calculated carrier effective mass, the deformation potential constant, and the corresponding carrier mobilities along the zigzag and armchair directions of the InS/$ZnIn_2S_4$ heterostructure. It can be seen that the hole mobility of the InS/$ZnIn_2S_4$ heterostructure is higher than that of electrons, and the hole mobility along the armchair direction reaches 6118.01 $cm^2\ V^{-1}\ s^{-1}$. The high carrier mobility characteristic gives it significant advantages in photovoltaic applications.

Fig. 3(a)–(c) present the projected band structure, projected density of states (DOS) and band alignment of the InS/$ZnIn_2S_4$ heterostructure. The heterostructure is a semiconductor with an indirect bandgap of 2.21 eV, where the CBM is at $\Gamma$ point, while the VBM is along the $\Gamma$–X line, which is smaller than both InS (2.47 eV) and $ZnIn_2S_4$ (2.73 eV). From the projected band structure and projected DOS, we find that the CBM is derived from the $ZnIn_2S_4$ layer and predominantly contributed by S and In atoms in the $ZnIn_2S_4$ layer, while the VBM is derived from the InS layer and primarily dominated by S atoms in the InS layer. Interestingly, we find that the InS/$ZnIn_2S_4$ heterostructure exhibits type-II band alignment, in which the CBM and VBM of the $ZnIn_2S_4$ layer are lower than those of the InS layer, also denoted as type-$II_1$ band alignment, as illustrated in Fig. 3(c). Moreover, when the external electric field is greater than 0.1 V $Å^{-1}$, the CBM and VBM of the $ZnIn_2S_4$ layer will be higher than those of the InS layer, resulting in another type-II alignment that is different from type-$II_1$, defined as type-$II_2$, as shown in Fig. 4(a). In addition, the calculated conduction band offset (CBO) and valence band offset (VBO) are 0.36 eV and 0.48 eV, respectively, both of which are smaller than those calculated using the Schottky–Mott model.[63] In the ideal Schottky–Mott limit, there is no interaction between the InS and $ZnIn_2S_4$ layer, the CBO and VBO are 0.44 eV and 0.70 eV, respectively. The type-II band alignment will significantly improve the efficiency of the separating photoinduced electron–hole pairs at the InS/$ZnIn_2S_4$ heterostructure's interface, in which the InS layer can act as an electron donor, while the $ZnIn_2S_4$ layer acts as an electron acceptors. The absorption spectra of the InS/$ZnIn_2S_4$ heterostructure, as well as isolated InS and $ZnIn_2S_4$ monolayers, are displayed (**https://www.wordhippo.com/what-is/another-word-for/display.html**) in Fig. 3(d). Compared with InS and $ZnIn_2S_4$ monolayer, the InS/$ZnIn_2S_4$ heterostructure demonstrates improved light absorption in the visible short-wavelength region (approximately 300–500 nm), which is mainly due to the bandgap narrowing after the formation of the heterostructure.

Considering that the InS/$ZnIn_2S_4$ heterostructure possesses $E_{in}$, type-II band alignment, and significant absorption coefficients in the ultraviolet and visible light bands, it may exhibit high-efficiency performance in solar cells. To study the $\eta$ of the InS/$ZnIn_2S_4$ heterostructure, we calculated the donor's bandgap ($E_g^d$), the ratio of the short-circuit current density to the AM1.5 solar flux ($J_{sc}/P_{solar}$), the conduction band offset ($\Delta E_c$), open circuit voltage ($V_{oc}$), and $\eta$, as listed in Tables S2 and S3.† The $J_{sc}/P_{solar}$ and $V_{oc}$ of the InS/$ZnIn_2S_4$ heterostructure are 0.087 and 1.91 V, respectively, resulting in a $\eta$ of 10.80%.

In practical applications, applying an external electric field (gate voltage) can modulate the characteristics of a given material. Here, we study the impact of a vertical electric field on the electronic band structure and band alignment of the InS/$ZnIn_2S_4$ heterostructure. The projected band structures and

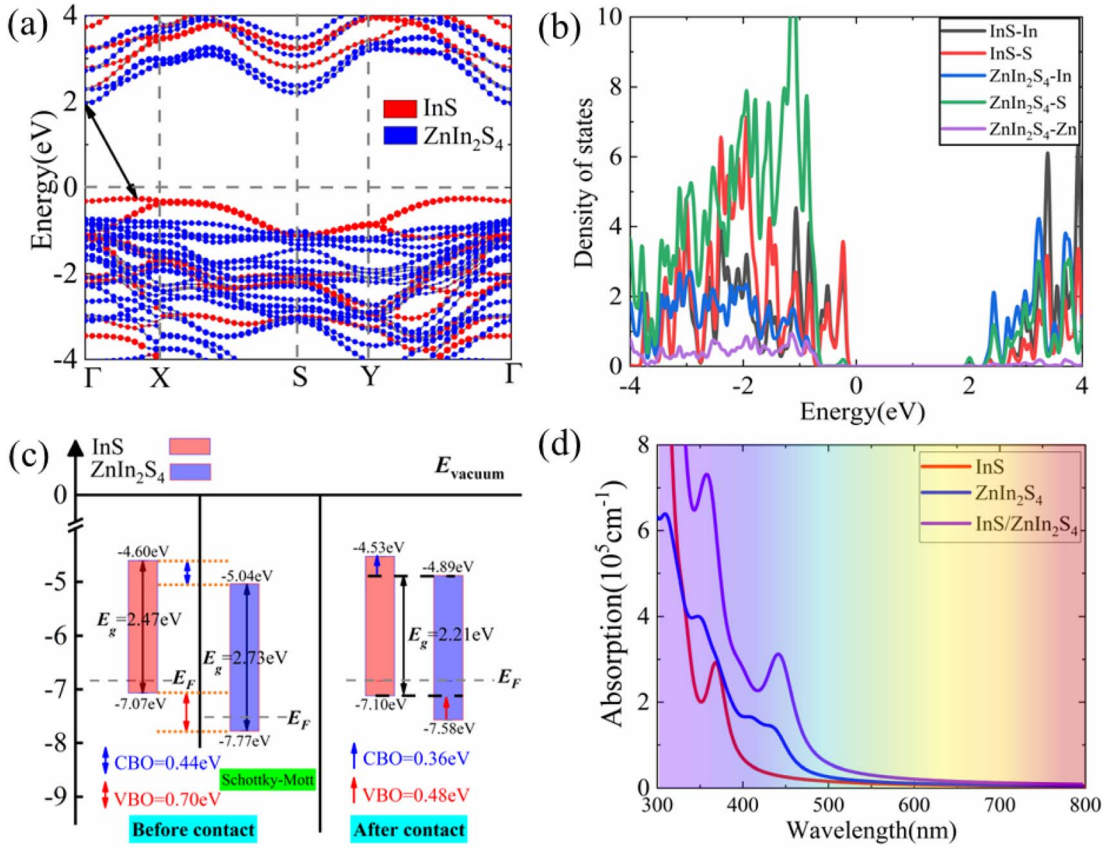


Fig. 3 The projected band structure (a), projected DOS (b), band alignment (c), and absorption spectra (d) of the InS/$ZnIn_2S_4$ heterostructure using the vacuum energy levels as a common energy reference. $E_g$ and $E_F$ denote the energies of the bandgap and Fermi energy levels, respectively. The CBO and VBO are represented by blue and red arrows, respectively.

band alignments of the InS/$ZnIn_2S_4$ heterostructure under vertical electric fields ($E_\perp$) ranging from −0.4 to 0.3 V Å$^{-1}$ are presented in Fig. S2† and 4(a), where the direction of the positive electric field is set to point from the InS layer to $ZnIn_2S_4$ layer. We also calculate the interlayer charge transfer ($\Delta Q$) of the InS/$ZnIn_2S_4$ heterostructure under different $E_\perp$, as depicted in Fig. 4(c).

Under the positive $E_\perp$, the direction of $E_{in}$ is opposite to that of $E_\perp$, and the band edge position of $ZnIn_2S_4$ layer will shifts upward with respect to that of the InS layer. When $0 < E_\perp < 0.05$ V Å$^{-1}$, the direction of the total electrical field ($E_t$) is the same as $E_{in}$, and there is a charge transfer from $ZnIn_2S_4$ to InS. The CBM and VBM of the $ZnIn_2S_4$ layer are both lower than those of the InS layer, and the heterostructure maintains a type-II$_1$ band alignment. With increasing $E_\perp$, the amount of $\Delta Q$ will decrease, and the CBO and VBO will both decrease. When $0.05 < E_\perp < 0.09$ V Å$^{-1}$, the direction of $E_t$ is same as that for $E_\perp$, and there will be a charge transfer from InS to $ZnIn_2S_4$. The CBM of the $ZnIn_2S_4$ layer is higher than that of the InS layer, and the VBM of the $ZnIn_2S_4$ layer is lower than that of the InS layer. The heterostructure thus changes into a straddling type-I band alignment. At this point, both the CBM and VBM of the InS/$ZnIn_2S_4$ heterostructure are contributed by the InS layer, making it easier to form electron hole pairs during electron transitions. This makes it potentially applicable in optoelectronic devices such as light-emitting diodes and lasers. With the increase of $E_\perp$, the amount of $\Delta Q$ will increase, the CBO will increase, and VBO will further decrease. When $0.09 < E_\perp < 0.3$V Å$^{-1}$, the direction of $E_t$ is also the same as that of $E_\perp$, and there will be a charge transfer from InS to $ZnIn_2S_4$. The CBM and VBM of the $ZnIn_2S_4$ layer both become higher than those of the InS layer, causing the heterostructure to transition into type-II$_2$ band alignment. With the increasing of $E_\perp$, the amount of $\Delta Q$ will increase, and the CBO and VBO will both increase.

Under a negative $E_\perp$, the $E_{in}$ and $E_\perp$ have the same direction, so the direction of $E_t$ consistently matches the $E_{in}$. There is a charge transfer ($\Delta Q$) from $ZnIn_2S_4$ to InS. The band edge position of the $ZnIn_2S_4$ layer moves downwards relative to that of the InS layer. With the increasing of the $E_\perp$, the $\Delta Q$ will increase gradually, and the CBO and VBO will both increase gradually. When $-0.35 < E_\perp < 0.0$V Å$^{-1}$, the CBM and VBM of the $ZnIn_2S_4$ layer both become lower than those of the InS layer, and the heterostructure can maintain a type-II$_1$ band alignment. When $E_\perp \geq 0.35$ V Å$^{-1}$, the VBM of InS becomes higher than the VBM and CBM of $ZnIn_2S_4$, and the band alignment of the heterostructure becomes type-III.

Moreover, the band gap size and type of the InS/$ZnIn_2S_4$ heterostructure are largely modulated by the electrical field, as displayed in Fig. 4(b). Under a positive $E_\perp$, as the $E_\perp$ is

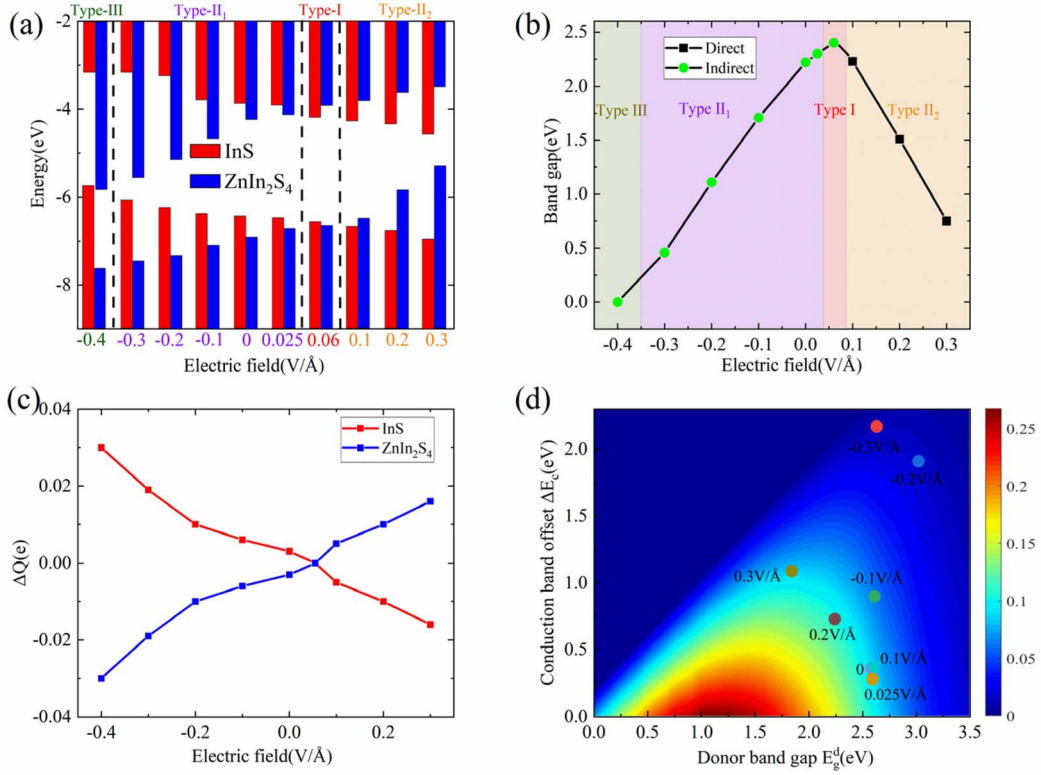


Fig. 4 The band alignments (a), band gaps (b), and charge transfer (c) of the InS/$ZnIn_2S_4$ heterostructure under different electric fields. (d) The $\eta$ of the InS/$ZnIn_2S_4$ heterostructure as a function of $\Delta E_c$ and $E_g^d$ under different electric fields.

increasing, the band gap of the InS/$ZnIn_2S_4$ heterostructure will firstly increase and then decrease. Under a negative $E_\perp$, the band gap of the InS/$ZnIn_2S_4$ heterostructure will monotonically decrease with increasing $E_\perp$. The heterostructure can also change to a direct bandgap semiconductor when $0.09 < E_\perp < 0.3\text{V Å}^{-1}$.

Next, we attempt to explore the $\eta$ of the InS/$ZnIn_2S_4$ heterostructure under different electric fields. As we know, to obtain a high $\eta$, a moderate $E_g^d$ is desirable. This is because the $V_{oc}$ will be enlarged and the $J_{sc}/P_{solar}$ will be reduced by increasing $E_g^d$. Secondly, the $\Delta E_c$ is as low as possible to reduce the energy loss and obtain a high $V_{oc}$. The calculated $E_g^d$, $J_{sc}/P_{solar}$, $\Delta E_c$, $V_{oc}$, and $\eta$ of the heterostructure with type-II alignment under different $E_\perp$ are listed in Table S2.† When $E_\perp < 0$, both $E_g^d$ and $\Delta E_c$ will be enlarged, which result in $J_{sc}/P_{solar}$ and $V_{oc}$ both being reduced, so the $\eta$ of the heterostructure becomes lower. When $E_\perp > 0$, $E_g^d$ will be enlarged and $\Delta E_c$ will be reduced. Subsequently, $E_g^d$ will be reduced and $\Delta E_c$ will be enlarged, which result in $J_{sc}/P_{solar}$ and $V_{oc}$ exhibiting different varying trends. Hence, the $\eta$ also exhibits a nonmonotonic variation. For $E_\perp = 0.2\text{ V Å}^{-1}$ and $0.3\text{ V Å}^{-1}$, the values of $E_g^d$ are 2.24 eV and 1.84 eV, respectively, which may theoretically result in large $\eta$. However, when $E_\perp > 0.2\text{ V Å}^{-1}$, the $\Delta E_c$ dramatically increases, reaching as high as 1.09 eV at $E_\perp = 0.3\text{ V Å}^{-1}$. This results in a significant decrease in $V_{oc}$. The $\eta$ can be increased up to 12.19% at $E_\perp = 0.2\text{ V Å}^{-1}$, as shown Fig. 4(d) and Table S2.†

Strain engineering can also modulate the electronic properties and $\eta$ of the semiconductor materials and their heterostructures.[17,19] Firstly, we attempt to examine the influence of biaxial strain ($\varepsilon$) on the electronic properties of the InS/$ZnIn_2S_4$ heterostructure. The biaxial strain ($\varepsilon$) is given by $\varepsilon = (a - a_0)/a_0$, where $a$ and $a_0$ represent the lattice constants of the strained and unstrained heterostructure, respectively. The strength of $\varepsilon$ ranging from −3% to 4% is considered, where a negative (positive) sign refers to compressive (tensile) strain. An increase in total energy is observed by applying a tensile or compressive strain, and the change in total energy is fitted to a quadratic curve, as depicted in Fig. 5(c). The electronic structure and band offset of the InS/$ZnIn_2S_4$ heterostructure under different $\varepsilon$ are given in Fig. S3† and 5.

Under tensile strain, as the $\varepsilon$ increases, the VBM of InS moves up and the CBM of $ZnIn_2S_4$ moves down, and the band gap of the InS/$ZnIn_2S_4$ heterostructure decreases linearly. At $\varepsilon = 4\%$, the bandgap decreases from 2.21 eV to 1.57 eV. Under compressive strain, as the $\varepsilon$ increases, the VBM of InS moves down and the CBM of $ZnIn_2S_4$ moves up, and the band gap of InS/$ZnIn_2S_4$ heterostructure increase linearly. At $\varepsilon = -3\%$, the bandgap of the InS/$ZnIn_2S_4$ heterostructure is increased from 2.21 eV to 2.60 eV. Moreover, for $-3\% < \varepsilon < 4\%$, the InS/$ZnIn_2S_4$ heterostructure always maintains a type-$II_1$ band alignment, along with an indirect band gap. The InS/$ZnIn_2S_4$ heterostructure can maintain a stable Type II alignment under biaxial strain ranging from −3% to 4%, suggesting its potential as a stable candidate material for solar cells.

Next, we calculate the $E_g^d$, $J_{sc}/P_{solar}$, $\Delta E_c$, $V_{oc}$, and $\eta$ of the InS/$ZnIn_2S_4$ heterostructure under different $\varepsilon$, as summarized in

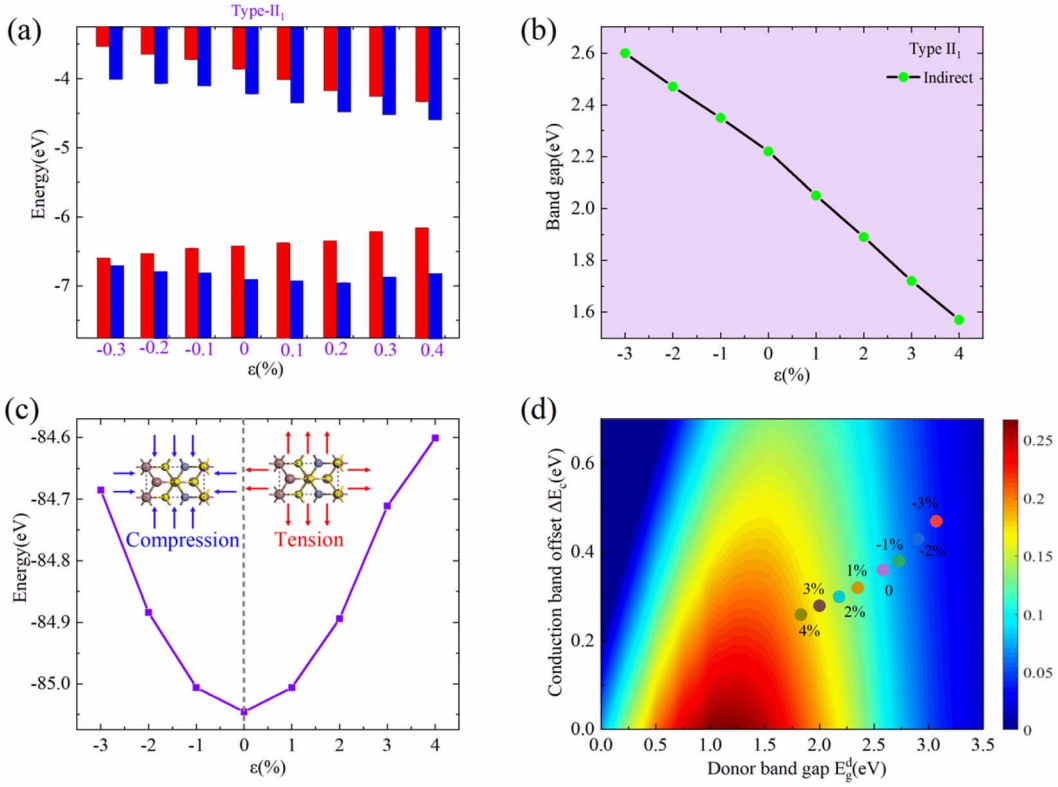


Fig. 5 The band alignments (a), band gaps (b), and the total energy (c) of the InS/$ZnIn_2S_4$ heterostructure under different biaxial strains. (d) The $\eta$ of the InS/$ZnIn_2S_4$ heterostructure as a function of $\Delta E_c$ and $E_g^d$ under different biaxial strains.

Table S3.† Under tensive strain, $E_g^d$ and $\Delta E_c$ decrease linearly with increasing strain, which result in the $J_{sc}/P_{solar}$ being enlarged and the $V_{oc}$ being reduced. Furthermore, the $\eta$ values of the InS/$ZnIn_2S_4$ heterostructure are enlarged. When $\varepsilon = 4\%$, a high $\eta$ of 20.80% was achieved, as displayed in Fig. 5(d) and Table S3.† Under compressive strain, $E_g^d$ and $\Delta E_c$ also increase linearly with increasing strain, which result in the $J_{sc}/P_{solar}$ being reduced and the $V_{oc}$ being increased. However, the $\eta$ values of the InS/$ZnIn_2S_4$ heterostructure are significantly reduced. When $\varepsilon = -3\%$, the $\eta$ is reduced to 4.18%, as shown in Fig. 5(d) and Table S3.† Therefore, biaxial strain modulation could be an effective approach to increase the $\eta$.[64]

## 4. Conclusions

In summary, we propose the two-dimensional InS/$ZnIn_2S_4$ heterostructure, and examine its electronic and optical characteristics using first principles calculations, focusing particularly on the band alignment and PCE. The AA stacking configuration is the most energetically favorable, possessing an indirect band gap of 2.21 eV and a large optical absorption coefficient in the short-wavelength visible region, along with a type-$II_1$ band alignment. Additionally, a significant $\eta$ of 10.86% has been achieved. The band alignment and $\eta$ of the InS/$ZnIn_2S_4$ heterostructure are largely modulated by applying an external electrical field or biaxial strain. The transformation of the band alignment from type-$II_1$ to type-I or type-$II_2$ can be induced by an external electric field, resulting in a further increase in $\eta$ up to 12.19% at a positive $E_\perp = 0.2$ V Å$^{-1}$. The type-$II_1$ band alignment remains stable within a critical biaxial strain of 4%, and a high $\eta$ of 20.80% is achieved under a tensile strain of $\varepsilon = 4\%$. This work is expected to provide new inspiration for improving solar cells with high PCE based on 2D InS/$ZnIn_2S_4$ heterostructures.

## Data availability

The data supporting this study have been included within the article and its ESI.† Additional data will be made available on reasonable request.

## Author contributions

Hui-Ying Liu: data curation (equal); formal analysis (equal); investigation (equal); writing – original draft (equal). Heng-Fu Lin: conceptualization (equal); formal analysis (equal); investigation (equal); supervision (equal); writing – review & editing (equal). Lu-Ya Xu: data curation (equal); formal analysis (equal); Ting-Ping Hou: conceptualization (equal); formal analysis (equal); investigation (equal); supervision (equal); writing – review & editing (equal). Nan-shu Liu: conceptualization (equal); formal analysis (equal); investigation (equal); supervision (equal); writing – review & editing (equal).

## Conflicts of interest

The authors have no conflicts of interest.

## Acknowledgements

This work was supported by the National Natural Science Foundation of China (12374191, 12204534), Fundamental Research Funds for the Central Universities (SWU-KQ24053) and Knowledge Innovation Program of Wuhan-Shuguang Project (No. 2023010201020404). This work was also supported by the computing time award at the High Performance Computing Center of Wuhan University of Science and Technology.

## References

1 Y. Cui, H. Yao, L. Hong, T. Zhang, Y. Tang, B. Lin, K. Xian, B. Gao, C. An, P. Bi, W. Ma and J. Hou, *Natl. Sci. Rev.*, 2020, **7**, 1239–1246.
2 Y. Cui, H. Yao, J. Zhang, K. Xian, T. Zhang, L. Hong, Y. Wang, Y. Xu, K. Ma, C. An, C. He, Z. Wei, F. Gao and J. Hou, *Adv. Mater.*, 2020, **32**, 1908205.
3 Z. Yu and L. Sun, *Adv. Energy Mater.*, 2015, **5**, 1500213.
4 H. Wu, K. Yang, Y. Si, W. Huang, W. Hu and G. Huang, *Phys. Status Solidi RRL*, 2019, **13**, 1800565.
5 Y. Chen, P. Ye, Z.-G. Zhu, X. Wang, L. Yang, X. Xu, X. Wu, T. Dong, H. Zhang, J. Hou, F. Liu and H. Huang, *Adv. Mater.*, 2017, **29**, 1603154.
6 K. Liang, T. Huang, K. Yang, Y. Si, H.-Y. Wu, J.-C. Lian, W.-Q. Huang, W.-Y. Hu and G.-F. Huang, *Phys. Rev. Appl.*, 2021, **16**, 054043.
7 R. Yan, S. Fathipour, Y. Han, B. Song, S. Xiao, M. Li, N. Ma, V. Protasenko, D. A. Muller, D. Jena and H. G. Xing, *Nano Lett.*, 2015, **15**, 5791–5798.
8 K. Datta and Q. D. Khosru, *J. Comput. Electron.*, 2017, **16**, 228–239.
9 J.-R. Zhang, X.-Z. Deng, B. Gao, L. Chen, C.-T. Au, K. Li, S.-F. Yin and M.-Q. Cai, *Catal. Sci. Technol.*, 2019, **9**, 4659–4667.
10 M. Z. Bellus, M. Li, S. D. Lane, F. Ceballos, Q. Cui, X. C. Zeng and H. Zhao, *Nanoscale Horiz.*, 2016, **2**, 31–36.
11 K. R. Williams, B. T. Diroll, N. E. Watkins, X. Rui, A. Brumberg, R. F. Klie and R. D. Schaller, *J. Am. Chem. Soc.*, 2019, **141**, 5092–5096.
12 Y. Wang, Q. Wang, X. Zhan, F. Wang, M. Safdar and J. He, *Nanoscale*, 2013, **5**, 8326–8339.
13 Y. Almadori, N. Bendiab and B. Grévin, *ACS Appl. Mater. Interfaces*, 2018, **10**, 1363–1373.
14 K. S. Novoselov, A. K. Geim, S. V. Morozov, D. Jiang, Y. Zhang, S. V. Dubonos, I. V. Grigorieva and A. A. Firsov, *Science*, 2004, **306**, 666–669.
15 M. C. Lemme, D. Akinwande, C. Huyghebaert and C. Stampfer, *Nat. Commun.*, 2022, **13**, 1392.
16 A. Chaves, J. G. Azadani, H. Alsalman, D. R. Da Costa, R. Frisenda, A. J. Chaves, S. H. Song, Y. D. Kim, D. He, J. Zhou, A. Castellanos-Gomez, F. M. Peeters, Z. Liu, C. L. Hinkle, S.-H. Oh, P. D. Ye, S. J. Koester, Y. H. Lee, Ph. Avouris, X. Wang and T. Low, *npj 2D Mater. Appl.*, 2020, **4**, 29.
17 Z. Cheng, R. Cao, K. Wei, Y. Yao, X. Liu, J. Kang, J. Dong, Z. Shi, H. Zhang and X. Zhang, *Adv. Sci.*, 2021, **8**, 2003834.
18 C. Sheng, X. Dong, Y. Zhu, X. Wang, X. Chen, Y. Xia, Z. Xu, P. Zhou, J. Wan and W. Bao, *Adv. Funct. Mater.*, 2023, **33**, 2304778.
19 K. S. Novoselov, A. Mishchenko, A. Carvalho and A. H. Castro Neto, *Science*, 2016, **353**, aac9439.
20 P. V. Pham, S. C. Bodepudi, K. Shehzad, Y. Liu, Y. Xu, B. Yu and X. Duan, *Chem. Rev.*, 2022, **122**, 6514–6613.
21 Y. Yu, S. Hu, L. Su, L. Huang, Y. Liu, Z. Jin, A. A. Purezky, D. B. Geohegan, K. W. Kim, Y. Zhang and L. Cao, *Nano Lett.*, 2015, **15**, 486–491.
22 X. Li, L. Tao, Z. Chen, H. Fang, X. Li, X. Wang, J.-B. Xu and H. Zhu, *Appl. Phys. Rev.*, 2017, **4**, 021306.
23 M. Shanmugam, R. Jacobs-Gedrim, E. S. Song and B. Yu, *Nanoscale*, 2014, **6**, 12682–12689.
24 M. M. Furchi, A. Pospischil, F. Libisch, J. Burgdörfer and T. Mueller, *Nano Lett.*, 2014, **14**, 4785–4791.
25 Y. Gong, S. Lei, G. Ye, B. Li, Y. He, K. Keyshar, X. Zhang, Q. Wang, J. Lou, Z. Liu, R. Vajtai, W. Zhou and P. M. Ajayan, *Nano Lett.*, 2015, **15**, 6135–6141.
26 M.-L. Tsai, S.-H. Su, J.-K. Chang, D.-S. Tsai, C.-H. Chen, C.-I. Wu, L.-J. Li, L.-J. Chen and J.-H. He, *ACS Nano*, 2014, **8**, 8317–8322.
27 K. Lai, H. Li, Y.-K. Xu, W.-B. Zhang and J. Dai, *Phys. Chem. Chem. Phys.*, 2019, **21**, 2619–2627.
28 H. Sun, Z. Wang and Y. Wang, *AIP Adv.*, 2017, **7**, 095120.
29 H.-F. Lin, H.-Y. Liu, M. Wang, S.-S. Wang, T.-P. Hou and K.-M. Wu, *Phys. Chem. Chem. Phys.*, 2022, **24**, 4425–4436.
30 Z. Wang, K. Xu, Y. Li, X. Zhan, M. Safdar, Q. Wang, F. Wang and J. He, *ACS Nano*, 2014, **8**, 4859–4865.
31 P. Hu, Z. Wen, L. Wang, P. Tan and K. Xiao, *ACS Nano*, 2012, **6**, 5988–5994.
32 K. Xu, L. Yin, Y. Huang, T. A. Shifa, J. Chu, F. Wang, R. Cheng, Z. Wang and J. He, *Nanoscale*, 2016, **8**, 16802–16818.
33 S. Demirci, N. Avazlı, E. Durgun and S. Cahangirov, *Phys. Rev. B*, 2017, **95**, 115409.
34 G. W. Mudd, S. A. Svatek, T. Ren, A. Patanè, O. Makarovsky, L. Eaves, P. H. Beton, Z. D. Kovalyuk, G. V. Lashkarev, Z. R. Kudrynskyi and A. I. Dmitriev, *Adv. Mater.*, 2013, **25**, 5714–5718.
35 S. Lei, L. Ge, S. Najmaei, A. George, R. Kappera, J. Lou, M. Chhowalla, H. Yamaguchi, G. Gupta, R. Vajtai, A. D. Mohite and P. M. Ajayan, *ACS Nano*, 2014, **8**, 1263–1272.
36 M. Brotons-Gisbert, D. Andres-Penares, J. Suh, F. Hidalgo, R. Abargues, P. J. Rodríguez-Cantó, A. Segura, A. Cros, G. Tobias, E. Canadell, P. Ordejón, J. Wu, J. P. Martínez-Pastor and J. F. Sánchez-Royo, *Nano Lett.*, 2016, **16**, 3221–3229.
37 A. Rawat, R. Ahammed, D. N. Jena, M. K. Mohanta and A. De Sarkar, *J. Phys. Chem. C*, 2019, **123**, 12666–12675.

38 R.-B. Luo, Q.-J. Liu, D.-H. Fan and Z.-T. Liu, *Appl. Surf. Sci.*, 2022, **605**, 154739.
39 M. A. Mohebpour, B. Mortazavi, T. Rabczuk, X. Zhuang, A. V. Shapeev and M. B. Tagani, *Phys. Rev. B*, 2022, **105**, 134108.
40 S. Zhang, Z. Zhang, Y. Si, B. Li, F. Deng, L. Yang, X. Liu, W. Dai and S. Luo, *ACS Nano*, 2021, **15**, 15238–15248.
41 L. Long, G. Lv, F. Pan, Z. Li, H. Zhu and D. Wang, *J. Phys. Chem. C*, 2023, **127**, 24077–24087.
42 Q. Ye, D. Xu, B. Cai, J. Lu, H. Yi, C. Ma, Z. Zheng, J. Yao, G. Ouyang and G. Yang, *Mater. Horiz.*, 2022, **9**, 2364–2375.
43 Z. Liang, Y.-Z. Liu, Z.-T. Gong, J.-Y. Li, Y.-S. Yao, Z.-K. Tang and X.-L. Wei, *Dalton Trans.*, 2024, **53**, 4729–4736.
44 X. Wang, X. Wang, T. Shi, A. Meng, L. Wang, S. Li, G. Li, X. Yu and Z. Li, *Sol. RRL*, 2023, **7**, 2200881.
45 G. Kresse and J. Furthmüller, *Phys. Rev. B:Condens. Matter Mater. Phys.*, 1996, **54**, 11169–11186.
46 G. Kresse and J. Furthmüller, *Comput. Mater. Sci.*, 1996, **6**, 15–50.
47 J. P. Perdew, K. Burke and M. Ernzerhof, *Phys. Rev. Lett.*, 1996, **77**, 3865–3868.
48 P. E. Blöchl, *Phys. Rev. B:Condens. Matter Mater. Phys.*, 1994, **50**, 17953–17979.
49 G. Kresse and D. Joubert, *Phys. Rev. B:Condens. Matter Mater. Phys.*, 1999, **59**, 1758–1775.
50 H. J. Monkhorst and J. D. Pack, *Phys. Rev. B: Solid State*, 1976, **13**, 5188–5192.
51 J. Paier, M. Marsman, K. Hummer, G. Kresse, I. C. Gerber and J. G. Angyán, *J. Chem. Phys.*, 2006, **124**, 154709.
52 S. Grimme, *J. Comput. Chem.*, 2006, **27**, 1787–1799.
53 M. Gajdoš, K. Hummer, G. Kresse, J. Furthmüller and F. Bechstedt, *Phys. Rev. B:Condens. Matter Mater. Phys.*, 2006, **73**, 045112.
54 M. C. Scharber, D. Mühlbacher, M. Koppe, P. Denk, C. Waldauf, A. J. Heeger and C. J. Brabec, *Adv. Mater.*, 2006, **18**, 789–794.
55 S. Bruzzone and G. Fiori, *Appl. Phys. Lett.*, 2011, **99**, 222108.
56 T. V. Vu, C. V. Nguyen, H. V. Phuc, A. A. Lavrentyev, O. Y. Khyzhun, N. V. Hieu, M. M. Obeid, D. P. Rai, H. D. Tong and N. N. Hieu, *Phys. Rev. B*, 2021, **103**, 085422.
57 T. Shen, J.-C. Ren, X. Liu, S. Li and W. Liu, *J. Am. Chem. Soc.*, 2019, **141**, 3110–3115.
58 I. A. Kibirev, A. V. Matetskiy, A. V. Zotov and A. A. Saranin, *Appl. Phys. Lett.*, 2018, **112**, 191602.
59 H. T. T. Nguyen, M. M. Obeid, A. Bafekry, M. Idrees, T. V. Vu, H. V. Phuc, N. N. Hieu, L. T. Hoa, B. Amin and C. V. Nguyen, *Phys. Rev. B*, 2020, **102**, 075414.
60 Q. Li, K.-Q. Chen and L.-M. Tang, *Phys. Rev. Appl.*, 2020, **13**, 014064.
61 B.-J. Wang, X.-H. Li, R. Zhao, X.-L. Cai, W.-Y. Yu, W.-B. Li, Z.-S. Liu, L.-W. Zhang and S.-H. Ke, *J. Mater. Chem. A*, 2018, **6**, 8923–8929.
62 K. Ren, W. Tang, M. Sun, Y. Cai, Y. Cheng and G. Zhang, *Nanoscale*, 2020, **12**, 17281–17289.
63 R. T. Tung, *Appl. Phys. Lett.*, 2014, **1**, 011304.
64 J. Zhao, Y. Li, G. Yang, K. Jiang, H. Lin, H. Ade, W. Ma and H. Yan, *Nat. Energy*, 2016, **1**, 1–7.